Chapter 4

The AZUR/EI-88 data base and radiation belt model

One of the tasks of WP 2.1 and 2.1R (Flight Data Comparisons) was to re-examine the old AZUR data set in order to build a proton belt model. The low altitude part of the NASA AP-8 MAX model is based entirely on the AZUR data set (Vette 1991b).

4.1 The AZUR mission

The AZUR satellite was launched on November 8, 1969, into a 102.9° inclination, sun-synchronous polar orbit with apogee 3145 km and perigee 384 km. The last telemetry data were recorded on June 18, 1970. Unfortunately, the data gathered after March 5, 1970 have been lost.

A cross sectional view of the AZUR satellite is shown in Fig. 4.1. The satellite was magnetically stabilized, with one axis aligned along the magnetic field direction, as shown in Fig. 4.2. The full orbital parameters are given in Table 4.1. The AZUR satellite has international reference 1969-097A No. 4221.

The instrument complement included detectors to measure the directional and omnidirectional fluxes of protons and electrons. These instruments and the high quality of the resulting measurements made the AZUR mission particularly well suited for the study of the trapped radiation environment, despite the short duration of the mission. The energetic proton measurements, which were collected during the maximum of Solar Cycle 20, were the basis for the low altitude part of the NASA model AP-8 MAX (Sawyer & Vette 1976).

4.1.1 Mission goals

The mission goals were the measurements of the following quantities:

1. directional proton intensities in several energy intervals between 0.25 and 100 MeV (two particle telescopes EI-88/1 and EI-88/2, PI D. Hovestadt);

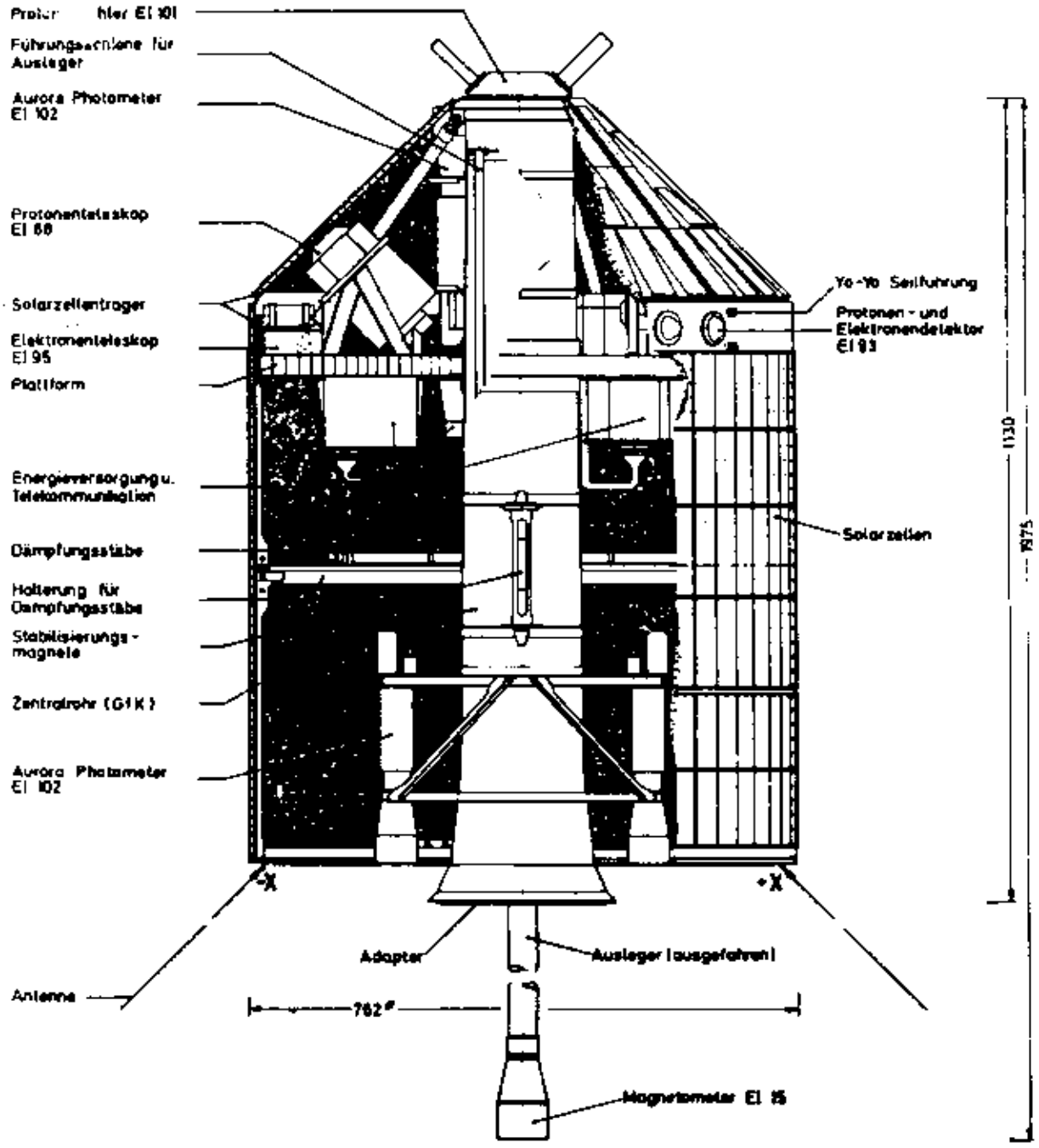

Figure 4.1. Cross section of the AZUR satellite

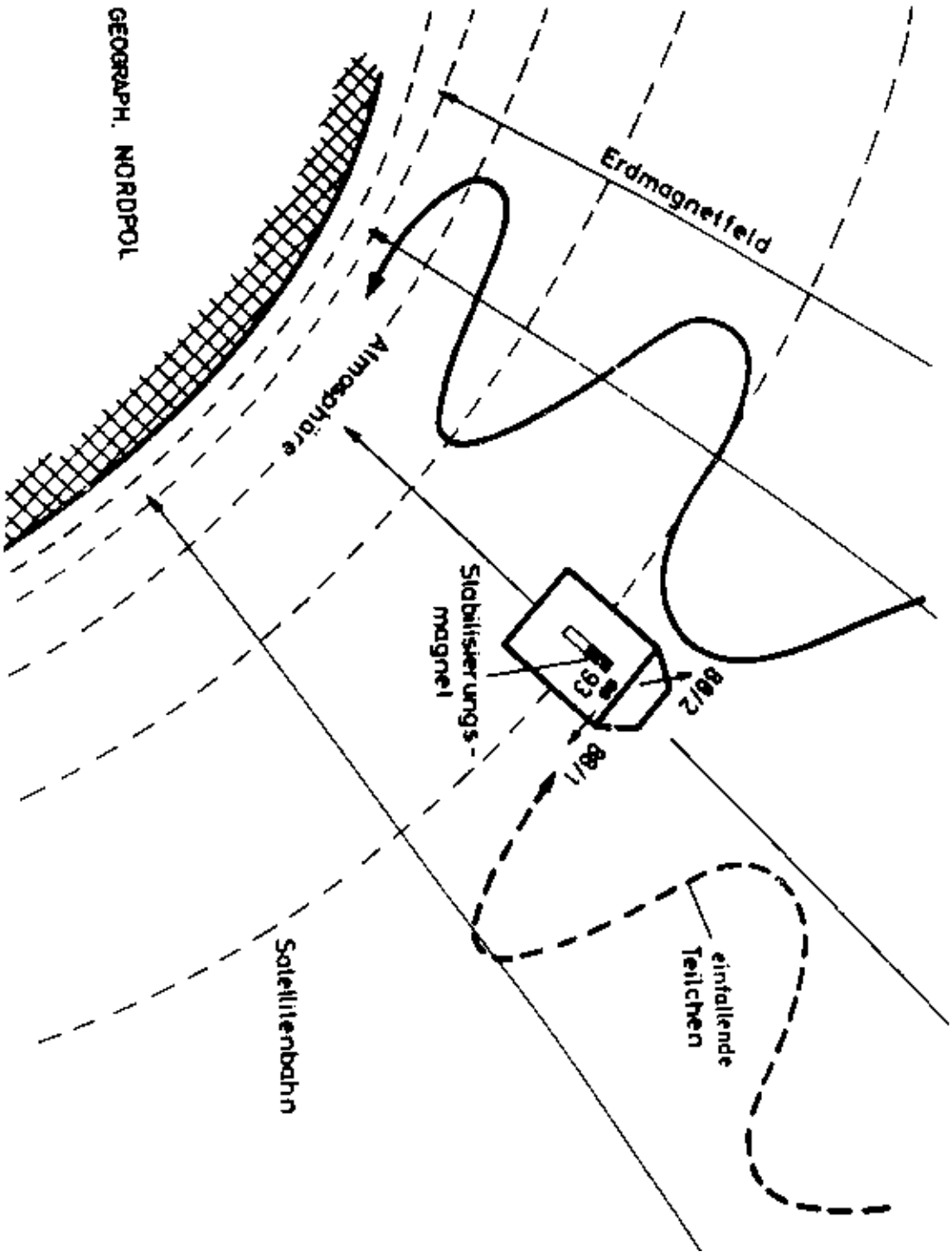

Figure 4.2. Representation of the orbital attitude of the AZUR satellite

Table 4.1. Orbital elements of the AZUR satellite

Orbital Element	Nominal Orbit	First Orbit
Semi-major axis (km)	8179.09	8142.80
Eccentricity	0.17337	0.16957
Inclination (deg)	102.671	102.975
Argument of perigee (deg)	161.801	161.906
Right ascension of ascending node (deg)	125.490	126.564
Period (m)	122.688	121.87603
Perigee height (km)	382.69	383.84
Apogee height (km)	3218.72	3145.43
Geocentric perigee latitude at injection (deg)	17.741 N	17.617 N
Precession of perigee (deg/day)	1.667	1.671
Precession of node line (deg/day)	0.96	

2. directional intensity of alpha particles in the energy range 6.5–19 MeV;
3. omnidirectional proton intensities in two energy ranges: 20–45 MeV and 40–80 MeV;
4. omnidirectional integral electron intensity above two thresholds: 1.5 and 4.0 MeV;
5. directional integral intensity of charged particles parallel, antiparallel and perpendicular to magnetic field lines, above 40 keV for electrons and 0.7 MeV for protons;
6. omnidirectional integral intensity of charged particles above two thresholds: 12 and 30 MeV for protons, 0.7 and 3.2 MeV for electrons;
7. optical emission by N_2^+ ($\lambda = 3914$ Å) and OI-N_2 ($\lambda = 2972$ Å);
8. transverse hydromagnetic waves with amplitudes above $5\,\gamma$ (magnetometer EI-15, PI G. Musmann).

The payload consisted of seven instruments. Descriptions of each instrument package can be found in Achtermann et al. (1970). In this study, we only use the measurements made by the two directional proton telescopes (EI-88/1 and EI-88/2), which are described below, and the magnetometer data.

4.1.2 The EI-88/1 and EI-88/2 proton telescopes

4.1.2.1 Measurement principle

The EI-88 experiment measures the directional proton flux in the energy range 1.5–100 MeV. Figure 4.3 is a cross section of the instrument. The aperture opening is constructed with a

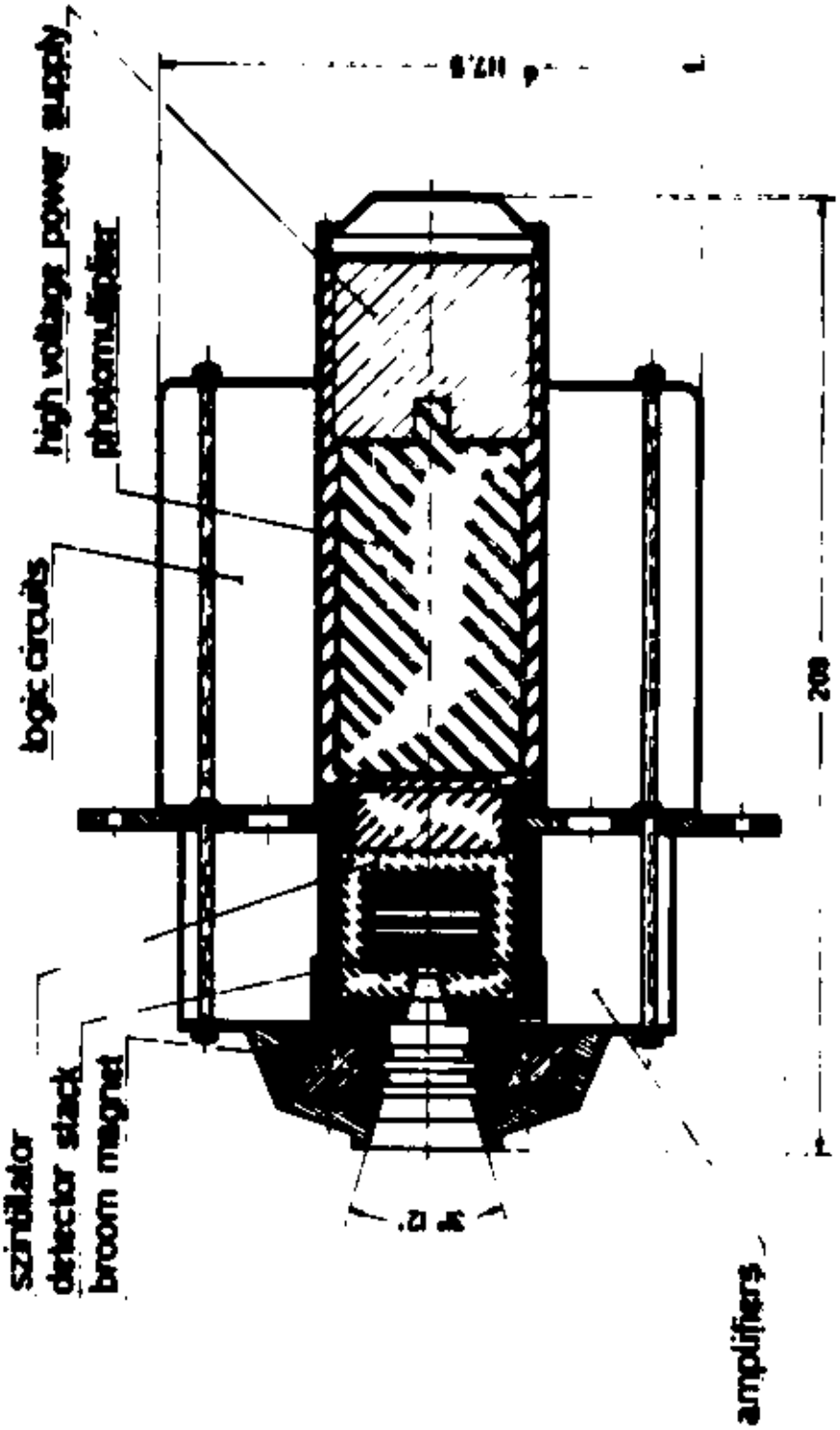

Figure 4.3. Cross section of the EI-88 intrument

number of Al and Ta collimators and is continued through a plastic scintillator surrounding the detectors and absorbers. The scintillator is connected to a photomultiplier by means of a plexiglass light conductor. The detectors respond to particle beams through the aperture opening. The energy dependent reach of the incident particles determines the number of detectors and absorbers they penetrate. Through the implementation of seven detectors and a treatment of the detector signal logic the total measurement range is divided into six energy ranges for protons and one channel for α particles. The anticoincidence rates are referred to as channel 8.

The lower limit of the detector range is determined by the thickness of the Ni foil placed before the scintillator, the thickness of the first detector, and the electronic threshold of the second detector. The Ni foil with thickness $1\,\mu \sim 8.9 \times 10^{-4} \mathrm{g\,cm^{-2}}$ serves to shield the scintillator and the detectors from incoming light. The upper energy limit of the instrument is given by the absorption thickness of the combined detector cage up to the aft inner wall of the scintillator. In addition to its role as upper energy limit for particles coming in through the aperture, the scintillator also tags particles that penetrate from outside the aperture through the combined shielding. An anticoincidence switch between scintillator and detectors prohibits these particles to be measured. In order to limit the impulse rate of the scintillator and, correspondingly, the dead time of the instrument, the electronics are constructed around the scintillator and the photomultiplier to provide additional shielding.

The electronic thresholds of the semiconductor detectors (see Table 4.2) are chosen sufficiently high so that electrons penetrating the aperture without scattering do not produce a signal. This arrangement does not rule out electrons undergoing multiple scattering and pile-up effects. Therefore, the instruments are equipped with a sweeping magnet which ensures that the influence of electrons on the ion count rates is negligible (Achtermann et al. 1970).

4.1.2.2 Detector layout and energy range

Figure 4.4 shows a cross section through the EI-88 sensors. The plastic scintillator surrounds an Al cage that contains the seven detectors and the three absorbers. The detector connectors are fed through holes in the scintillator and the closest Ta shield to the amplifiers, which are arranged around the detector cage. Figure 4.5 shows the energy deposited in the detectors as a function of the energy of the incident proton. The detector thresholds and switching logic yield the energy ranges for protons and α particles listed in Table 4.3.

The detectors EI-88/1 and EI-88/2 are identical except for a small difference in aperture angle, and thus geometric factor. The angular response function of the telescopes is discussed in Sect. 4.3.1. The integration time for both instruments is fixed at 10 s. Due to the slow spin rate of the satellite, this rather long integration time does not compromise the quality of the directional measurements.

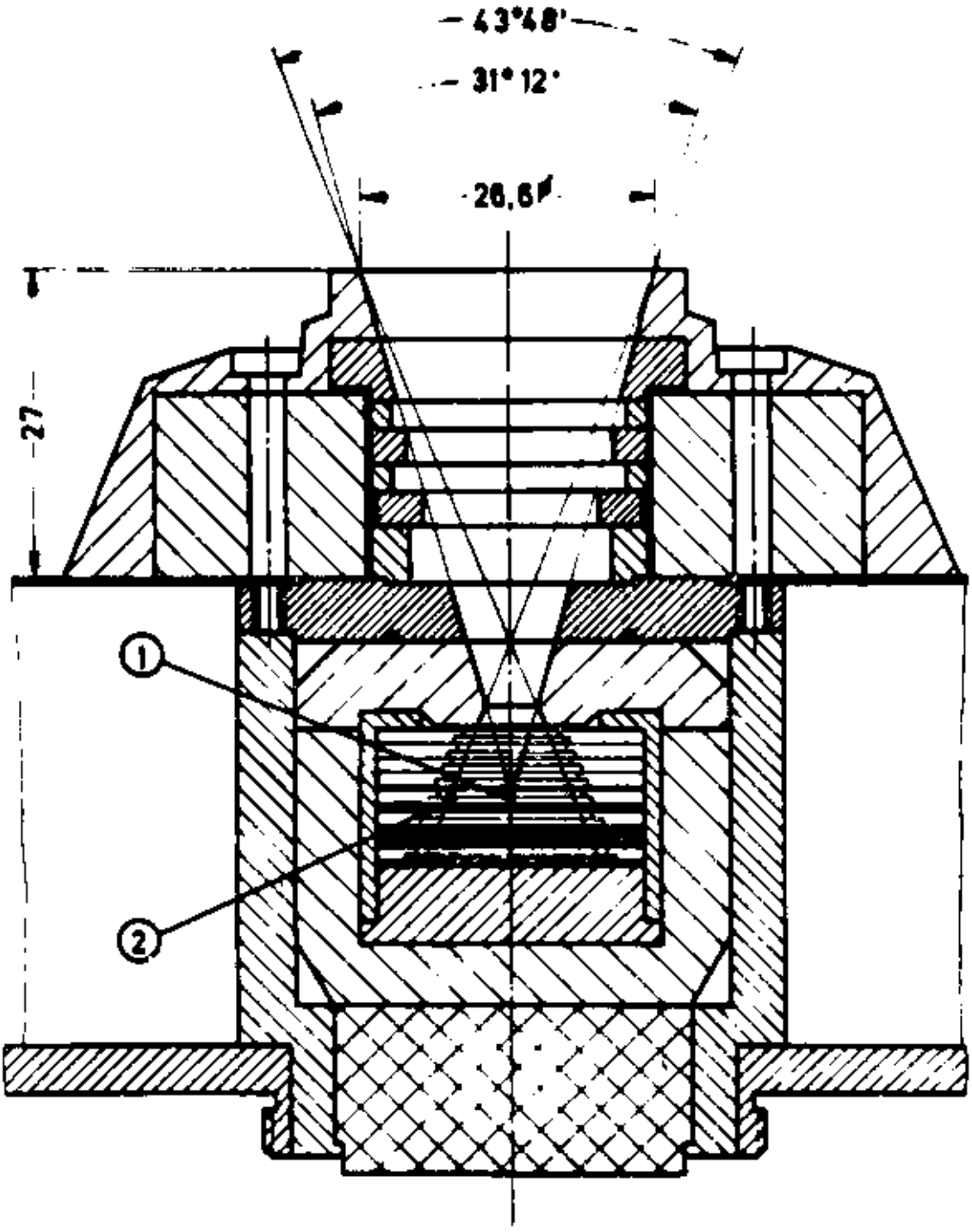

Figure 4.4. Cross section of the EI-88 sensors

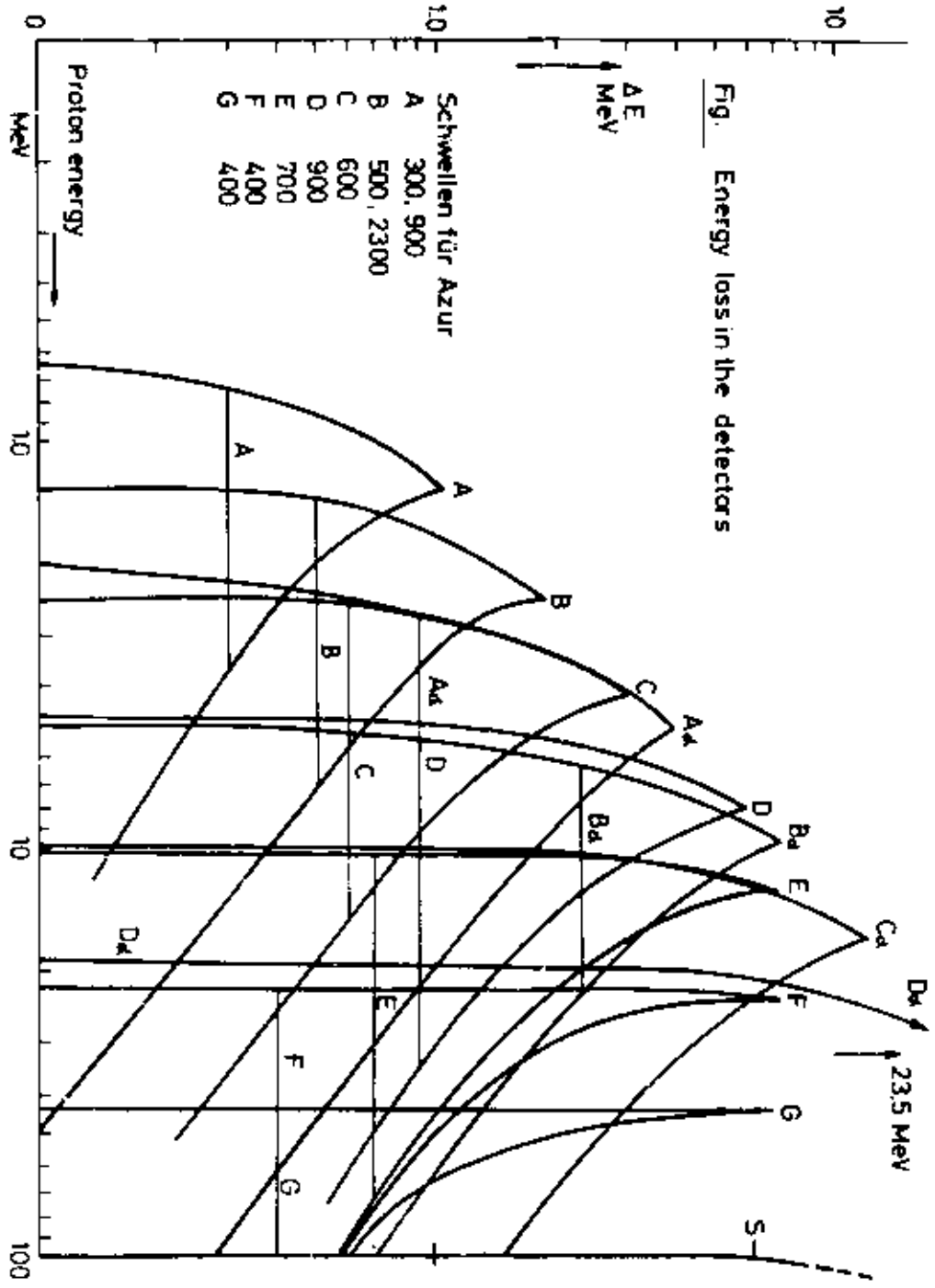

Figure 4.5. Energy deposited in the EI-88 detectors as a function of incident particle energy

Table 4.2. Detector and absorber characteristics of the EI-88 instruments

Detector	Absorber	Thickness (μ)	Electronics threshold (keV)
	Ni	1	
A		20	300, 900
B		50	500, 2300
C		100	600
	Al	30	
D		300	900
	Al	200	
E		400	700
	Cu	565	
	Al	30	
F		400	400
	Ta	1750	
G		400	400
	Ta	7050	

Table 4.3. Energy channels of the EI-88 instruments for protons and α particles

Channel	Logic	Particle	Energy range (MeV)
1	A B $\bar{\text{C}}$ $\bar{\text{S}}$	protons	1.5–2.7
2	A B $\bar{\text{D}}$ $\bar{\text{S}}$	α	6.0–19.0
3	B C $\bar{\text{D}}$ $\bar{\text{S}}$	protons	2.7–5.2
4	C D $\bar{\text{E}}$ $\bar{\text{S}}$	protons	5.2–10.4
5	D E $\bar{\text{F}}$ $\bar{\text{S}}$	protons	10.4–22.0
6	E F $\bar{\text{G}}$ $\bar{\text{S}}$	protons	22.0–48.8
7	F G $\bar{\text{S}}$	protons	48.8–104.0
8	S	anticoincidence	

4.2 The EI-88 data base

In this section we describe the downloading of the data sets to a DEC Alpha workstation running OpenVMS. The data analysis is performed with a series of IDL programmes and one FORTRAN programme [to calculate (B, L) values]. The different steps in the analysis procedure are outlined and the format of the final data base is described.

Table 4.4. Record structure of the AZUR tape identification files

Word	Content
1	1
2	Satellite Id. Nr. 6909701
3	Experiment Id. Nr. 889293
4	Tape Nr.
5–81	Spares

Table 4.5. Content of the AZUR tape pass header records

Word Nr.	Content	Representation
1	Type of record	Integer
2	Year of begin of pass	Integer
3	Day of begin of pass	Integer
4	Second of begin of pass	Integer
5	Year of end of pass	Integer
6	Day of end of pass	Integer
7	Second of end of pass	Integer
8	Orbit number at begin of pass	Integer
9	First character of station name	Character
10	Second character of station name	Character
11	Third character of station name	Character
12	Fourth character of station name	Character
13	Fifth character of station name	Character
14	K_{p}	Float
15–81	Spare	

4.2.1 Retrieval of the data sets

The data were sent to BIRA/IASB by NSSDC in the form of two magnetic tapes. Originally, the data were sent to NSSDC by MPE on 14 tapes, each tape containing a data file and a tape identification file. NSSDC merged the data set to two tapes containing 28 binary files in total: 14 data files and 14 identification files. The tapes are 9 track, 800 bpi, unlabelled, with `RECFM=VBS` and `BLKSIZE=9844`. These two tapes were read at BIRA/IASB on an Apollo workstation and the 28 files were then transferred by binary FTP to the Alpha workstation.

The tapes were written by a CYBER machine. The internal representation of floating numbers on this architecture differs from the representation on the Alpha hardware. In addition, al-

Table 4.6. Content of the AZUR tape data records

Word Nr.	Content	Representation
1	Type of record (pass header or data)	Integer
2	Quality	Integer
3	Year	Integer
4	Day	Integer
5	UT (ms)	Integer
6	LT hour	Integer
7	LT min	Integer
8	MLT hour	Integer
9	MLT min	Integer
10	Orbit Nr.	Integer
11	Spare	
12	Geographic latitude (deg)	Float
13	Geographic longitude (deg)	Float
14	Geographic distance (R_{E})	Float
15	Right ascension (deg)	Float
16	Declination (deg)	Float
17	Magnetic latitude (deg)	Float
18	Magnetic longitude (deg)	Float
19	L (R_{E})	Float
20	B (gauss)	Float
21	Λ (invariant latitude, deg)	Float
22	R (R_{E})	Float
23	Angle between satellite axis and **B** (deg)	Float
24	Azimuth with respect to **B** (deg)	Float
25	Aspect angle to sun (deg)	Float
26	Azimuth angle with respect to sun (deg)	Float
27	γ_1 Spin axis (geocentric, deg)	Float
28	γ_2 Spin axis (geocentric, deg)	Float
29	γ_3 Spin axis (geocentric, deg)	Float
30	B_x Magnetic field vector component (geocentric, deg)	Float
31	B_y Magnetic field vector component (geocentric, deg)	Float
32	B_z Magnetic field vector component (geocentric, deg)	Float
33	Spare	
34	Spare	
35	Spare	
36	Station (abbreviation to one character)	Character

Table 4.6. (continued)

Word Nr.	Content	Representation
37	Orbit counter	Integer
38	Record counter	Integer
39	Corrected orbit counter	Integer
40	Corrected record counter	Integer
41	EI-88/1 Channel 1 counts plus 1	Integer
42	EI-88/1 Channel 2 counts plus 1	Integer
43	EI-88/1 Channel 3 counts plus 1	Integer
44	EI-88/1 Channel 4 counts plus 1	Integer
45	EI-88/1 Channel 5 counts plus 1	Integer
46	EI-88/1 Channel 6 counts plus 1	Integer
47	EI-88/1 Channel 7 counts plus 1	Integer
48	EI-88/1 Channel 8 counts plus 1	Integer
49	EI-88/2 Channel 1 counts plus 1	Integer
50	EI-88/2 Channel 2 counts plus 1	Integer
51	EI-88/2 Channel 3 counts plus 1	Integer
52	EI-88/2 Channel 4 counts plus 1	Integer
53	EI-88/2 Channel 5 counts plus 1	Integer
54	EI-88/2 Channel 6 counts plus 1	Integer
55	EI-88/2 Channel 7 counts plus 1	Integer
56	EI-88/2 Channel 8 counts plus 1	Integer
57	EI-93 Channel 1 counts plus 1	Integer
58	EI-93 Channel 2 counts plus 1	Integer
59	EI-93 Channel 3 counts plus 1	Integer
60	EI-93 Channel 4 counts plus 1	Integer
61	EI-92 Channel 1 counts plus 1	Integer
62	EI-92 Channel 2 counts plus 1	Integer
63	EI-92 Channel 3 counts plus 1	Integer
64	EI-92 Channel 4 counts plus 1	Integer
65	EI-92 Channel 5 counts plus 1	Integer
66	EI-92 Channel 6 counts plus 1	Integer
67	EI-88/1 Detector current	Integer
68	EI-88/1 Logic	Integer
69	EI-88/2 Detector current	Integer
70	EI-88/2 Logic	Integer
71	EI-93 Detector current	Integer
72	EI-92 Detector current	Integer
73	Light in EI-92	Integer

Table 4.6. (continued)

Word Nr.	Content	Representation
74	Calibration mode	Integer
75	EI-88/1 Temperature	Integer
76	EI-88/1 Photomultiplier	Integer
77	EI-88/2 Temperature	Integer
78	EI-88/2 Photomultiplier	Integer
79	EI-93 Temperature	Integer
80	EI-92 Temperature	Integer
81	16 V Voltage	Integer

phanumeric information is coded in EBCDC on the CYBER. The IDL programme `tape.pro` reads in each data file, transforms the binary code to Alpha format and writes the resulting values to a set of new files in ASCII format. These files have names `TAPEnn.DAT` and reside in the main directory. Odd-numbered files are tape identification files (see Table 4.4 for their contents) and are not used in the data processing.

The even-numbered files contain the actual data (100 orbits per file). The data in each file are organised in passes (or contacts) between different ground stations. Each pass begins with a pass header record and is followed by the normal data records in chronological order. Each record, of both types, consists of 81 four byte words. The content of word nr. 1 specifies the record type. The contents of the pass header records and data records are given in Tables 4.5 and 4.6, respectively.

Word 2 of the data records identifies the data quality:

```
Word 2 = 0:  good
       = 1:  average
       = 2:  bad
```

Records flagged as `bad` were rejected in the data analysis. Words 3 to 40 contain auxiliary data. Words 41 to 66 contain the counting rates of the scientific data channels. The channels contain the counting rates plus 1, i.e. 1 means zero counts.

Words 67 to 81 contain housekeeping data of the experiments and the logical condition. Word 74 indicates `normal mode (=0)` or `calibration mode (=1)`. Words 68 and 70 contain the mode of operation of EI-88/1 and EI-88/2, respectively:

```
Word 68 (70) = 0:  data channels of EI-88/1 and EI-88/2
                   contain count rates of Table~1.3
             = 1:  channels contain single rates of
                   detectors A to G and anticoincidence
```

The modes of operation alternate in a fixed sequence of a period of 16 formats (10 s each): 14 formats designated with `0` are followed by 2 formats designated `1`. The first format with a `1` and the first format with a `0` are a mixture of coincidence and single rates and can therefore not be used. For the final data base all formats with a `1` were rejected.

4.2.2 Cleaning of the data sets

The next step in the data processing is the "cleaning" of the ASCII data files `TAPEnn.DAT` generated by `TAPE.PRO`. This routine reads in a data file `TAPEnn.DAT`, rejects bad data records and produces an output file `CLEANnn.DAT`. The records of the ASCII files produced by the programme `CLEAN.PRO` do not contain all the words listed in Table 4.6, in particular the data for EI-93 and EI-92 (words 57–66), housekeeping data (words 67–81), and records 1, 11, 33–35, and 37–40 were not copied. The first line in each `CLEANnn.DAT` file consists of column headers.

The effect of the cleaning programme is shown in Figs. 4.6 and 4.7, which show the raw and cleaned count rates for a sample of channel 4 data in file `TAPE4.DAT`.

4.2.2.1 Rejection criteria

Not all the records in the data files are valid measurement records. Bad or contaminated records and housekeeping records were identified and not included in the final data files. Below, we describe the different rejection criteria.

Calibration mode Data records with the calibration mode flag (word 74) set to one can be safely rejected.

Quality flag Data records with quality flag (word 2) equal to two are of bad quality (or don't contain data) and can be safely rejected.

Pitch angle not defined A value -7.0 for the angle between the satellite axis and **B** (word 23) indicates a problem with the magnetometer data. These data records are rejected.

Mixed mode records The modes of operation of EI-88 alternate in a fixed sequence of a period of 16 formats (10 s each): 14 formats designated with `0` are followed by 2 formats designated `1`. The first format with a `1` and the first format with a `0` are a mixture of coincidence and single rates and can therefore not be used. The combined rejection criterion is that each record is rejected for which word 68 differs from word 68 in the previous record, or for which word 70 differs from word 68 in the previous record. The first record in every data file is rejected as well.

Satellite conditions The operational conditions of the satellite and instruments are recorded in the housekeeping records 67–81. Data records for which the actual values of the following parameters deviate too much from the average (over the whole data file, except for

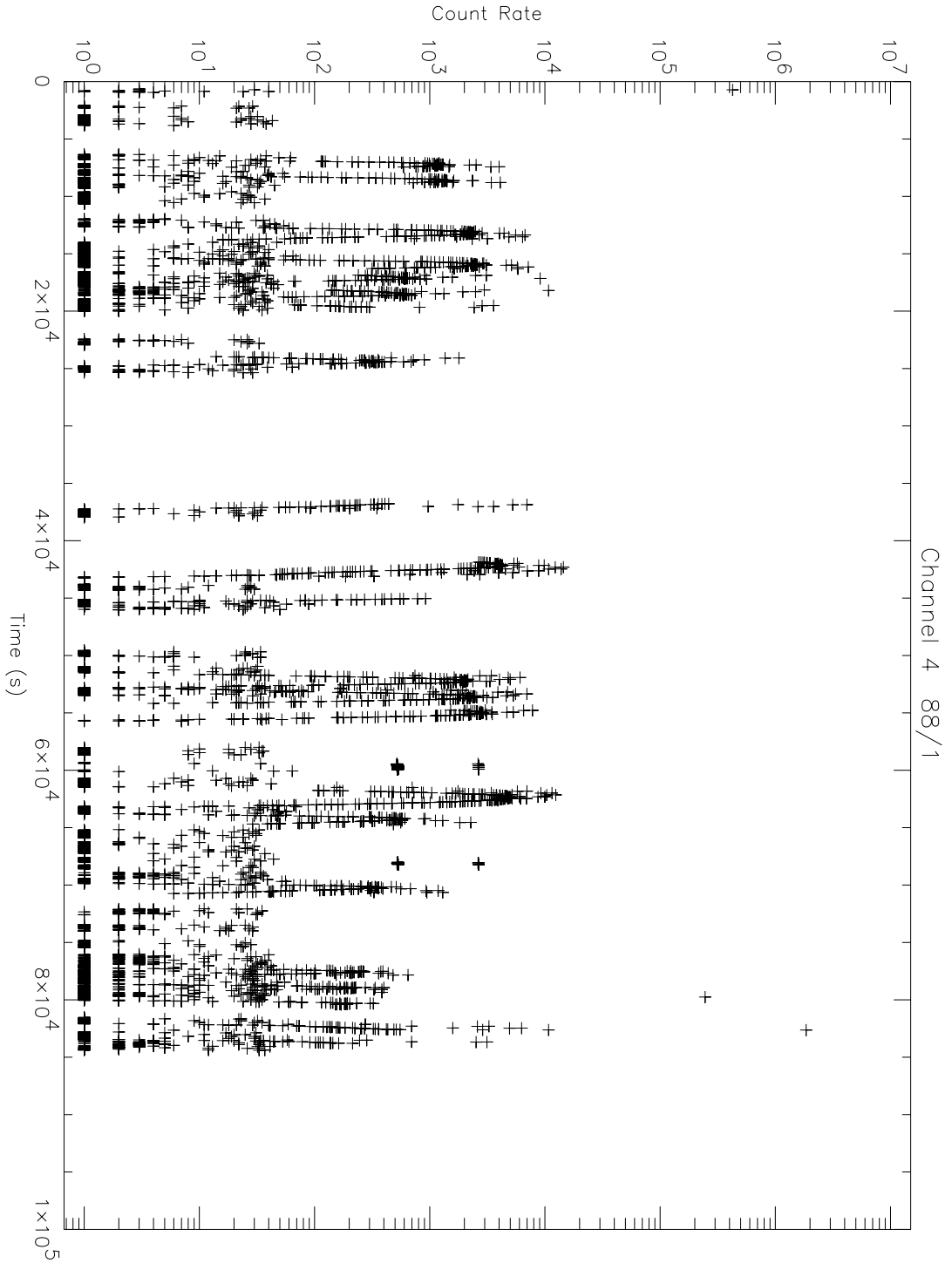

Figure 4.6. Sample of the raw EI-88/1 channel 4 count rates in data file TAPE4.DAT

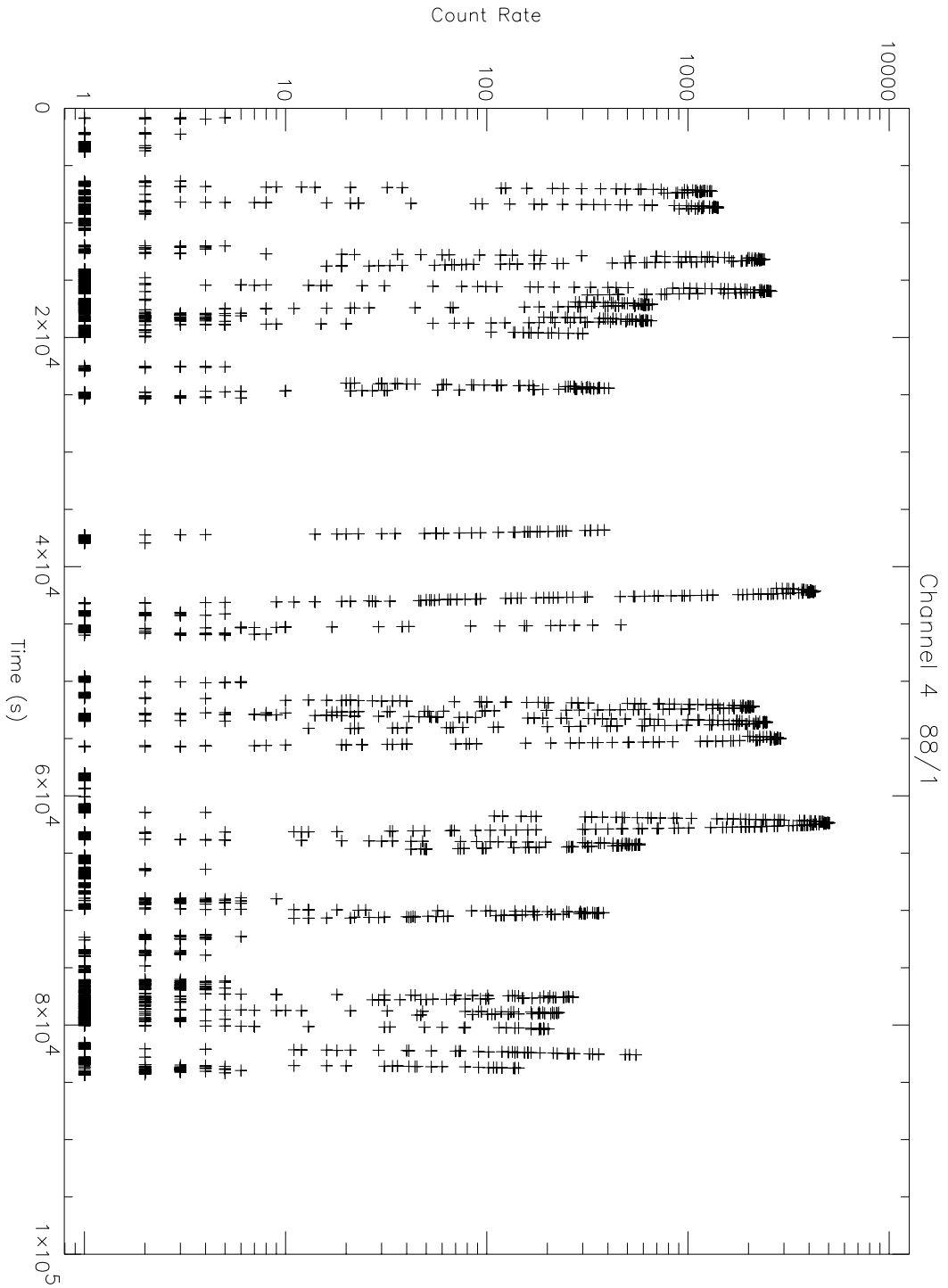

Figure 4.7. Sample of the EI-88/1 channel 4 count rates in data file `TAPE4.DAT` after running the cleaning programme

the records already flagged as suspect) value of the parameter are flagged, for each EI-88 detector separately: detector current, temperature, photomultiplier current, and 16 V voltage. If the record is flagged, the count rates for the corresponding detector are set to -1. On visual inspection of the time evolution of the individual data points, it was found that the record preceding a record with deviating conditions was very often erroneous as well. Therefore, the records preceding (while checking that there are no gaps in the telemetry) bad condition records are flagged as well.

Deviation from neighbouring values The above "cleaning" criteria are able to identify most of the measurements that are invalid because of instrumental or telemetric effects. However, after a detailed inspection of time plots and listings of the cleaned data, some spurious data were still found. We did not find a criterion to identify these deviating points unambiguously, and decided on another scheme to remove them: after applying all the above criteria, each count rate (for each channel and detector separately) is compared to the average of the preceding and succeeding count rate. If the middle count rate is more than a factor five (a value of five turned out to be a good compromise between not rejecting too many data points and not rejecting enough spurious points) above the average count rate, it is set to -1. On average, about a few dozen measurements per channel and per data file are rejected by this criterion.

Abnormally high values After applying the selection criteria described above, a small number of data points still deviate from the surrounding points (in contrast to "neighbouring points", by "surrounding points" are meant points separated from a given point by at least two ten-second interval) when plotted as a function of time, in the sense that these suspect points have count rates in one or more detectors that are much higher (up to two orders of magnitude) than those of the neighbouring points. We inspected time plots of all the data, for each detector separately, and identified the remaining suspect data points by eye. Since there are only very few of these points (a few dozen over the whole data base) and they deviate clearly from the neighbouring points, we feel confident in eliminating them. Also, the averages and standard deviations of the data after removing these points improve substantially. "Removing a point" in this context means that the count rate of the specific detector channel is set to -1.

4.3 Model construction

In order to construct flux maps, count rates have to be converted to physical units (fluxes) and averaged over two-dimensional coordinate grids. The conversion to fluxes is an iterative process because of the finite aperture of the detectors, i.e. the true unidirectional flux has to be derived from the measured count rate in successive approximations, using the procedure outlined in Appendix A.

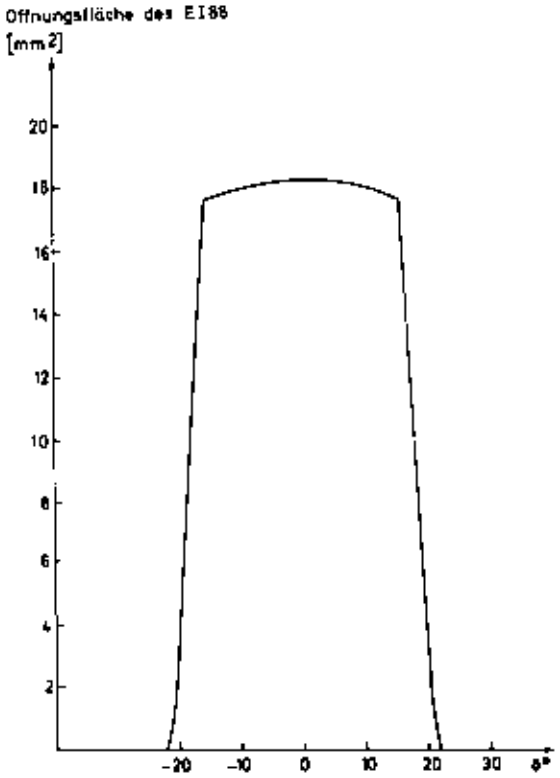

Figure 4.8. Measured effective area for the EI-88 detectors [from Achtermann et al. (1970)]

Table 4.7. Geometric factors and surface areas of the EI-88 sensors [from Haüsler (1972)]

Channel	$G\,(\mathrm{cm^2 sr})$	$A\,(\mathrm{cm^2})$	$G\,(\mathrm{cm^2 sr})$	$A\,(\mathrm{cm^2})$
	EI-88/1		**EI-88/2**	
1–5	0.0580	0.1817	0.0595	0.1864
6	0.0612	0.1917	0.0628	0.1967
7	0.0772	0.2418	0.0792	0.2481

4.3.1 Effective areas of the EI-88 detectors

The cone shape of the EI-88 detector stacks (see Fig. 4.4) ensures that lower-lying sensors are not obscured by the sensors above them. Therefore, for an ideal detector of this type each sensor should have the same effective area. Plots of the effective areas for different particle energies are shown for the various sensors in Häusler (1972, Figs. 8–10). Figure 8 in Achtermann et al. (1970)—reproduced in Fig. 4.8—shows the analytically derived effective area function that only depends on the detector geometry, and thus is valid (in the ideal case) for each sensor. Figure 10 in Achtermann et al. (1970) shows the measured effective area for 8 MeV protons

in channel 4, which corresponds closely to the analytical effective area. From measurements in a particle beam the authors conclude that for the first five channels the effective area is not dependent on energy. However, particles with higher energies (from about 34 MeV on) can penetrate the edge of the telescope shielding and part of the scintillator, and thus cause an enlargement of the geometric factor for channels 6 and 7. Häusler (1972) lists the geometric factors for the respective channels (see Table 4.7). In the analysis of the AZUR data, an analytic representation of the effective area function shown in Fig. 4.8 was used.

4.3.2 Selection of bin sizes

After a comparative study of several coordinate grids, it was found that an (E, L, α_0) grid is best suited for the data binning. As the equatorial pitch angle always ranges between $0°$ and $90°$, the (L, α_0) bins are rectangular regardless of the L range, which is not the case for other coordinate grids, such as (L, B).

The bin limits where chosen so that the measurements are distributed as evenly as possible over the bins. Firstly, a set of L values was selected. The AZUR orbit is such that the magnetic equator is only covered for $L \leq 1.6$. For higher L values, the range of equatorial pitch angles "seen" by the satellite rapidly diminishes with increasing L. Beyond $L = 3$, the coverage is too small to be useful for a radiation belt model, so we limit the model to $L = 3$.

After selecting the bin limits of the L grid, the whole database was binned in an (L, α_0) grid with equidistant spacing of the α_0 bin limits at $3°$. Then, the number of measurements falling in each α_0 bin was summed over the L bins, to obtain the total number of measurements in each α_0 bin. The cumulative number of measurements is shown in Fig. 4.9 as $\times$ symbols, and was fitted by a parabolic curve. Points on this curve which are equidistant in ordinate define a series of α_0 values. We have set the number of α_0 bins to 50, and derived the α_0 values corresponding to 50 equidistant intervals in cumulative number of measurements. The resulting values are the bin limits for a new α_0 grid, which is superimposed on Fig. 4.9, and listed in Table 4.8. In order to close the grid, the values $0°$ and $90°$ were added.

The database was then rebinned over the new (L, α_0) grid. The distribution of the measurements in channel 1 over the (L, α_0) map is shown in Fig. 4.10.

4.3.3 Correction for telescope field of view

The IDL programme `MODEL.PRO` reads in the flux averages created by `BINNING.PRO` and writes the final flux map `AZUR90.DAT` (we have only treated the EI-88/1 data). Since the AZUR data coverage in (L, α_0) space is not uniform, `MODEL.PRO` extends the equatorial pitch angle dependence where necessary to the equator ($\alpha_0 = 90°$). The extension is achieved by fitting, for each E and L bin, the function

$$j(\alpha_0, B_0) = \begin{cases} K \left(\dfrac{\sin \alpha_0}{\sqrt{B_0}} - \dfrac{1}{\sqrt{B_c}} \right) \exp \left[-\beta \left(\dfrac{\sin \alpha_0}{\sqrt{B_0}} - \dfrac{1}{\sqrt{B_c}} \right) \right] & \alpha_0 \geq \alpha_{0L} \\ 0 & \alpha_0 \leq \alpha_{0L} \end{cases} \tag{4.1}$$

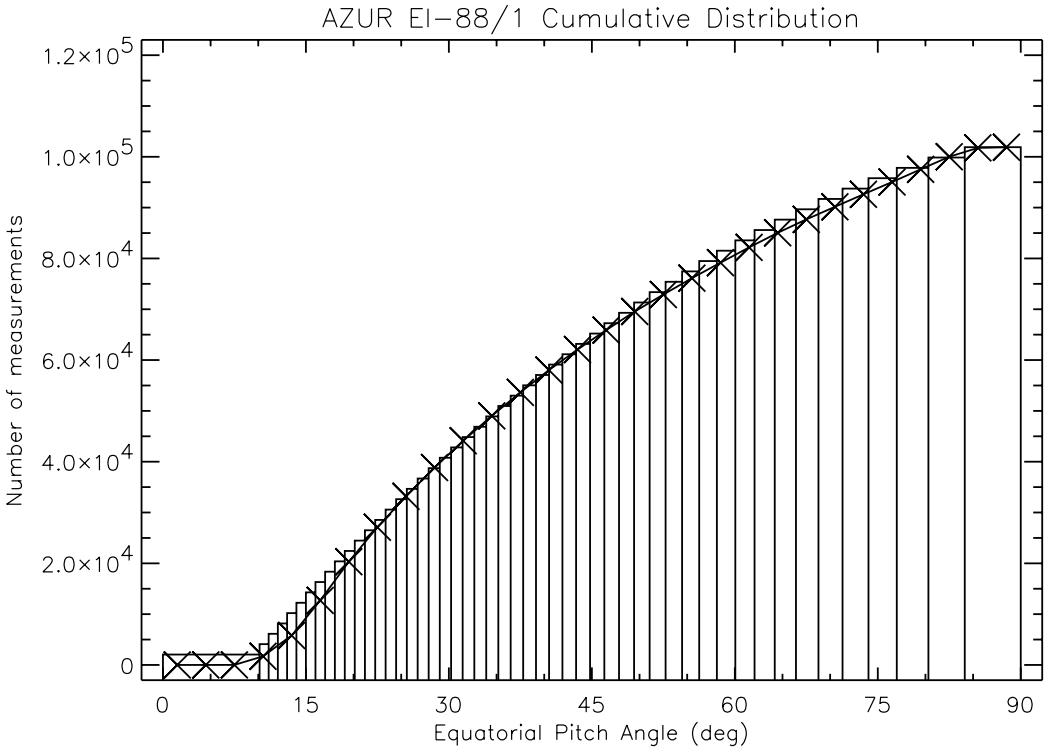

Figure 4.9. Cumulative distribution of AZUR EI-88/1 measurements in α_0 bins. The symbols $\times$ represent evenly spaced bins of width $3°$, while the final bins are represented in histogram style.

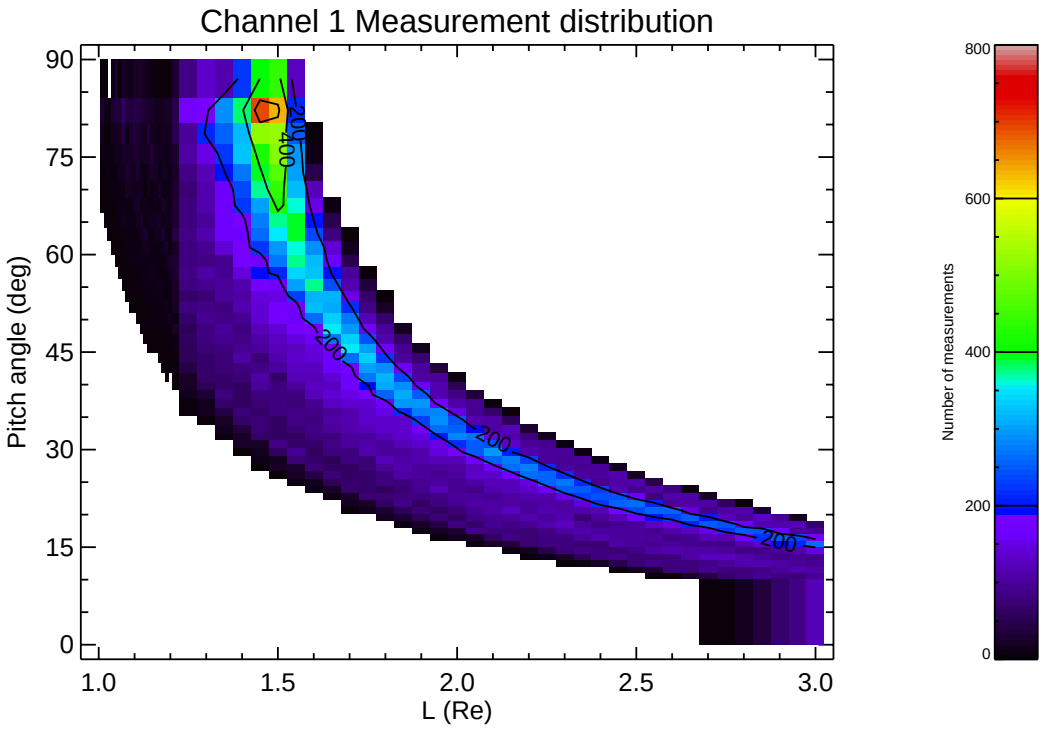

Figure 4.10. (L, α_0) Map of the number of measurements for channel 1

Table 4.8. (E, L, α_0) Bin limits for the PAB97 model grid

E Limits (MeV)	L Limits (R_{E})	α_0 Limits (deg)
1.5	1.005	0.0000
2.7	1.015	10.1397
5.2	1.025	11.0914
10.4	1.035	12.0522
22.0	1.045	13.0235
48.8	1.055	14.0045
104.0	1.065	14.9966
	1.075	15.9996
	1.085	17.0134
	1.095	18.0394
	1.105	19.0770
	1.115	20.1277
	1.125	21.1908
	1.135	22.2679
	1.145	23.3591
	1.155	24.4643
	1.165	25.5853
	1.175	26.7215
	1.185	27.8749
	1.195	29.0455
	1.205	30.2336
	1.225	31.4412
	1.275	32.6680
	1.325	33.9164
	1.375	35.1861
	1.425	36.4796
	1.475	37.7977
	1.525	39.1410
	1.575	40.5126
	1.625	41.9128
	1.675	43.3450
	1.725	44.8099
	1.775	46.3115
	1.825	47.8518
	1.875	49.4333
	1.925	51.0610
	1.975	52.7376
	2.025	54.4695
	2.075	56.2616
	2.125	58.1198
	2.175	60.0540
	2.225	62.0722
	2.275	64.1886
	2.375	66.4169
	2.425	68.7793
	2.475	71.3020
	2.525	74.0215
	2.575	76.9961
	2.625	80.3106
	2.675	84.1227
	2.725	90.0000
	2.775	
	2.825	
	2.875	
	2.925	
	2.975	
	3.025	

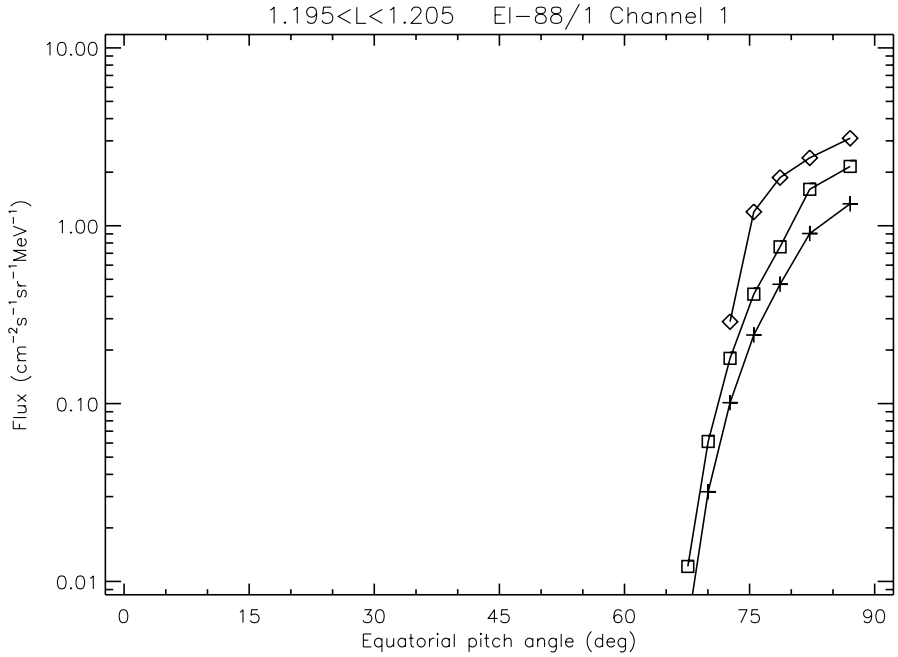

Figure 4.11. Uncorrected flux averages (□) for EI-88/1 channel 1, $L = 1.2$. The symbols $+$ represent the flux predicted by means of Eq. (A.19), and the symbols $\diamond$ are the corrected bin averages.

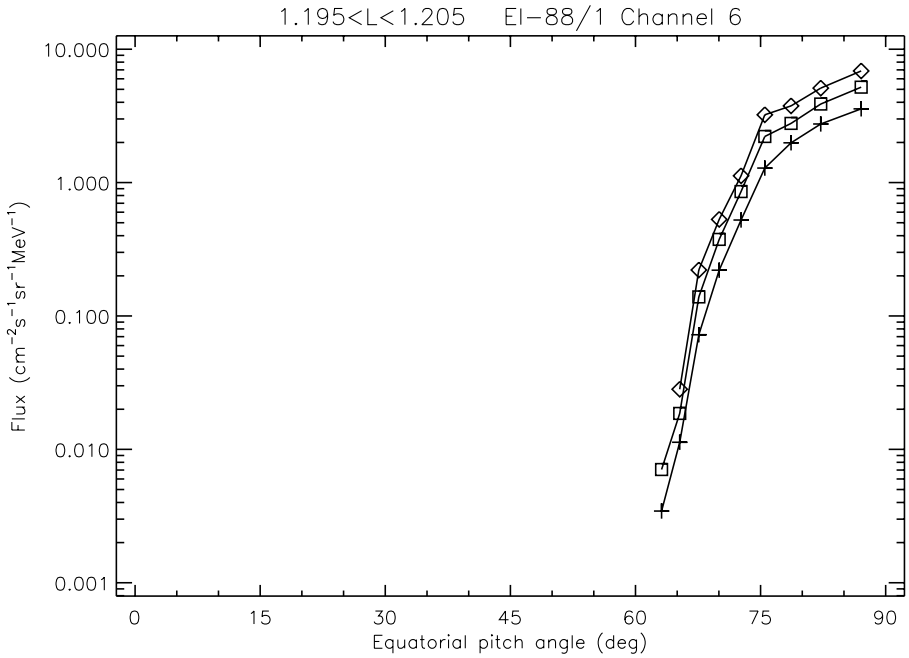

Figure 4.12. Same as Fig. 4.11, for channel 6 and $L = 1.2$

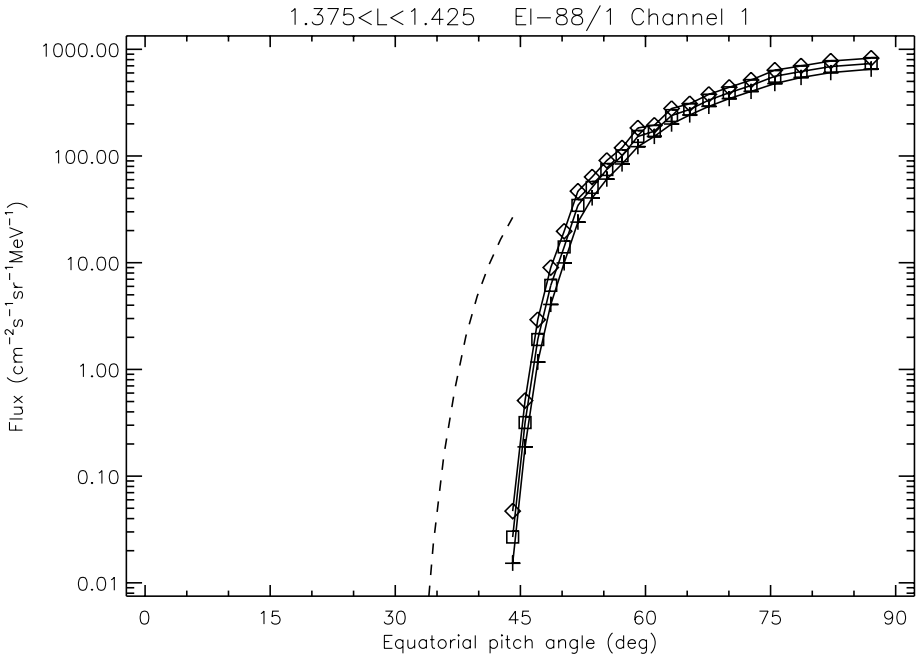

Figure 4.13. Uncorrected flux averages for EI-88/1 (perpendicular to the magnetic field) channel 1, $L = 1.4$. The symbols have the same meaning as in Fig. 4.11. The dashed line represents the flux predicted by means of Eq. (A.19) for detector EI-88/2 (at an angle of 45° to the magnetic field).

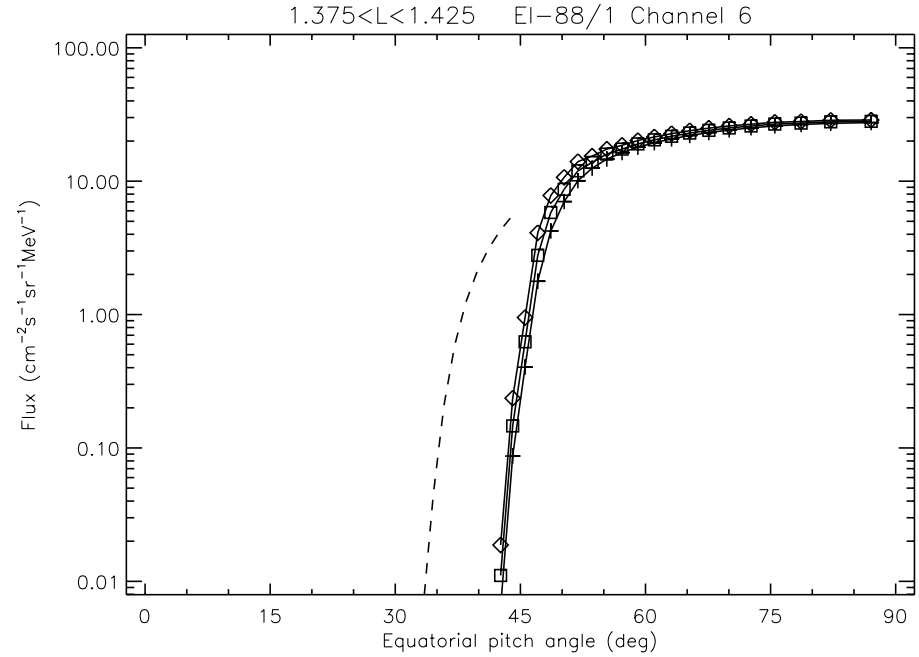

Figure 4.14. Same as Fig. 4.13, for channel 6 and $L = 1.4$

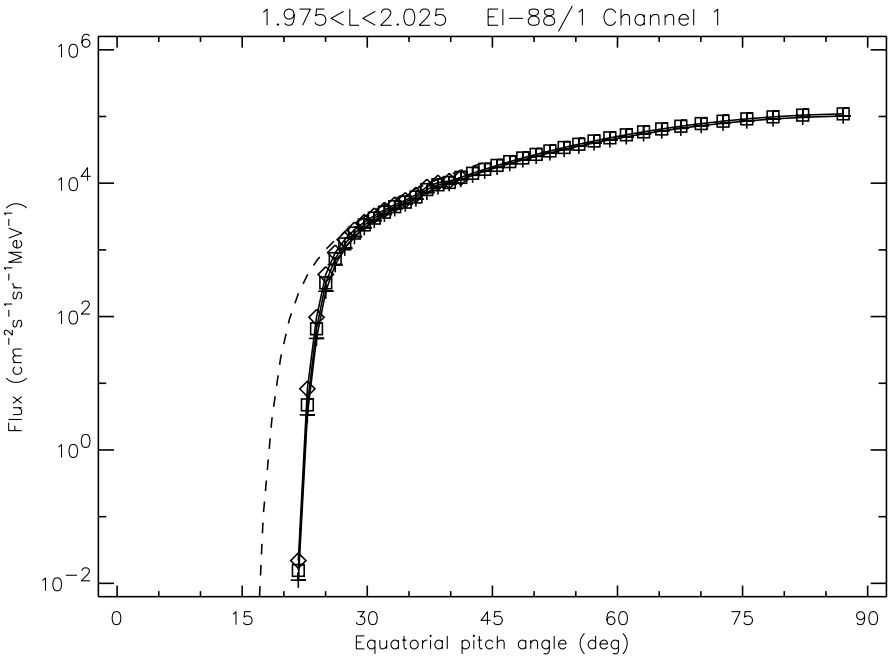

Figure 4.15. Same as Fig. 4.13, for channel 1 and $L = 2.0$

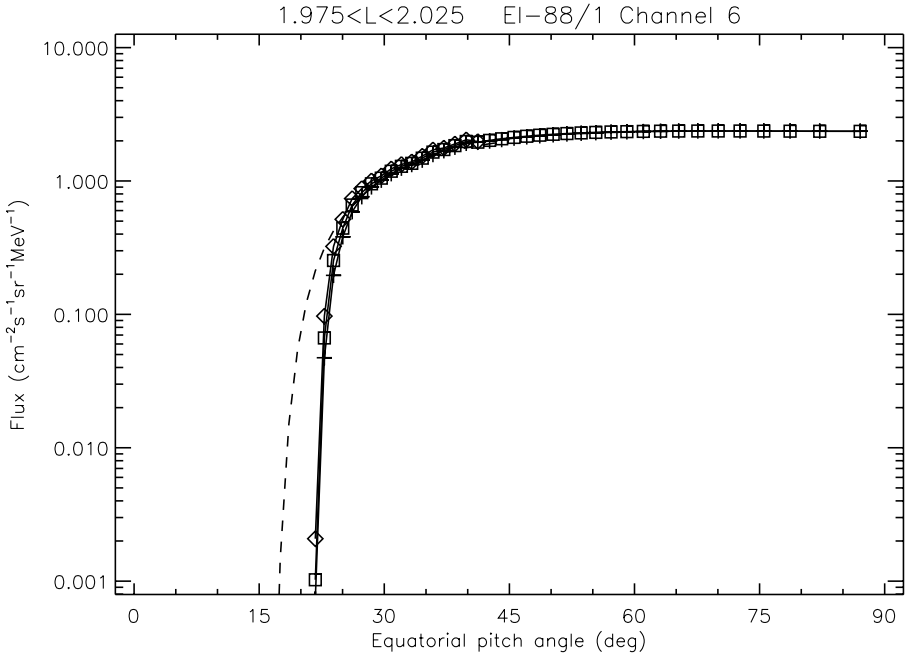

Figure 4.16. Same as Fig. 4.13, for channel 6 and $L = 2.0$

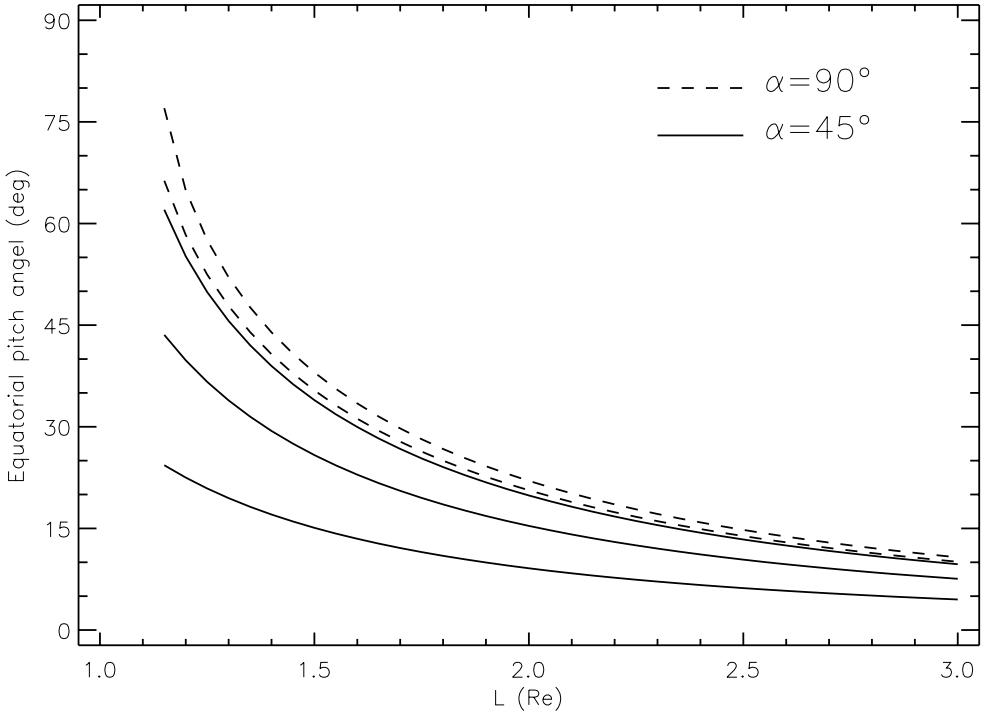

Figure 4.17. Comparison of the equatorial pitch angles subtended by the EI-88/1 and EI-88/2 detectors

(Badhwar & Konradi 1990, Heynderickx & Lemaire 1993) to the non-zero fluxes in the bin averages, and replacing zero flux values outside the loss cone with the values obtained with the fit function. When not enough bin averages are different from zero, the fit is replaced by the pitch angle dependence of AP-8 MAX, scaled to the flux value of the bin closest to the equator. The extension of the pitch angle coverage is necessary for the application of Eq. (A.19), as the integration in α_0 can extend beyond the equatorial pitch angle range covered by the measurements. `MODEL.PRO` Also has a feature to replace non-zero flux values with the fit function, which is necessary when a bin average clearly deviates from the surrounding points.

Figures 4.11–4.16 show the uncorrected average fluxes ($\Box$) as a function of α_0 for channels 1 and 6 for detector EI-88/1, for three values of L. Superimposed on the figures are the fluxes obtained by means of Eq. (A.19) ($+$), and the bin means obtained by averaging the fluxes after one iteration of the correction procedure outlined in Sect. A.2 ($\diamond$).

The correction for the telescope opening angle clearly depends on the L value and on the energy channel. The correction is largest where the flux dependence on α_0 is steepest, i.e. for the smallest L values and the lowest energy channels.

The reason we have not included the EI-88/2 measurements in the model, is their limited coverage in (L, α_0) space. In addition, these measurements can not be corrected with the method outlined in Sect. A.2. To illustrate this point, we have used Eq. (A.19) to calculate the flux seen by EI-88/2 for the cases represented in Figs. 4.11–4.16 and superimposed the resulting values in these figures as dashed lines. The fluxes as seen by EI-88/2 are shifted towards

the loss cone with respect to the real flux distribution (for $L = 1.2$, EI/88-2 does not see any flux at all). The correction procedure used for EI-88/1 would result in a correction factor equal to zero for almost all measurements. The difference between the integrated fluxes for the respective telescopes is caused by the different α_0 intervals covered by the two instruments, as shown in Fig. 4.17.

4.3.4 Final flux map

The bin averages obtained after one iteration of the procedure outlined above are used to build the final flux map. The α_0 coverage of the final bin averages is not extended toward the equator. Instead, for (L, α_0) bins not covered by the measurements, the flux is set to -1, so that the software using the model map can exclude the corresponding points. The resulting coverage in (L, α_0) space is illustrated in Figs. 4.18 and 4.20 for the lowest and highest energy channels. The fitting procedure described in Sect. 4.3.3 is applied, however, to correct bin averages that clearly deviate from the pitch angle dependence defined by the other bins (the number of corrections is very small).

The final flux map is then transformed into a `BLOCK DATA` file by means of the programme `MODTOBD.FOR`. This programme also transforms differential into integral fluxes. The implementation of the new AZUR model (called PAB97) in `UNIRAD` is described in Technical Note 10.

4.3.5 Comparison to AP-8

Figures 4.18 and 4.20 show two flux maps of the PAB97 model in (L, α_0) space, together with the directional AP-8 MAX maps for the same grid values. Figures 4.19 and 4.21 show the ratios of the AP-8 MAX values to the PAB97 model values. It can be seen that for the lowest L values the PAB97 fluxes are smaller than the corresponding AP-8 MAX fluxes by a factor of about two. For higher L values, the agreement between the two models is satisfactory.

Another way of comparing the PAB97 model to AP-8 consists of drawing world maps of fluxes at fixed altitude. Figures 4.22 and 4.23 show the distributions of the PAB97 and AP-8 MAX proton flux >50 MeV at an altitude of 500 km, respectively. Again, the PAB97 flux is lower than the AP-8 MAX flux.

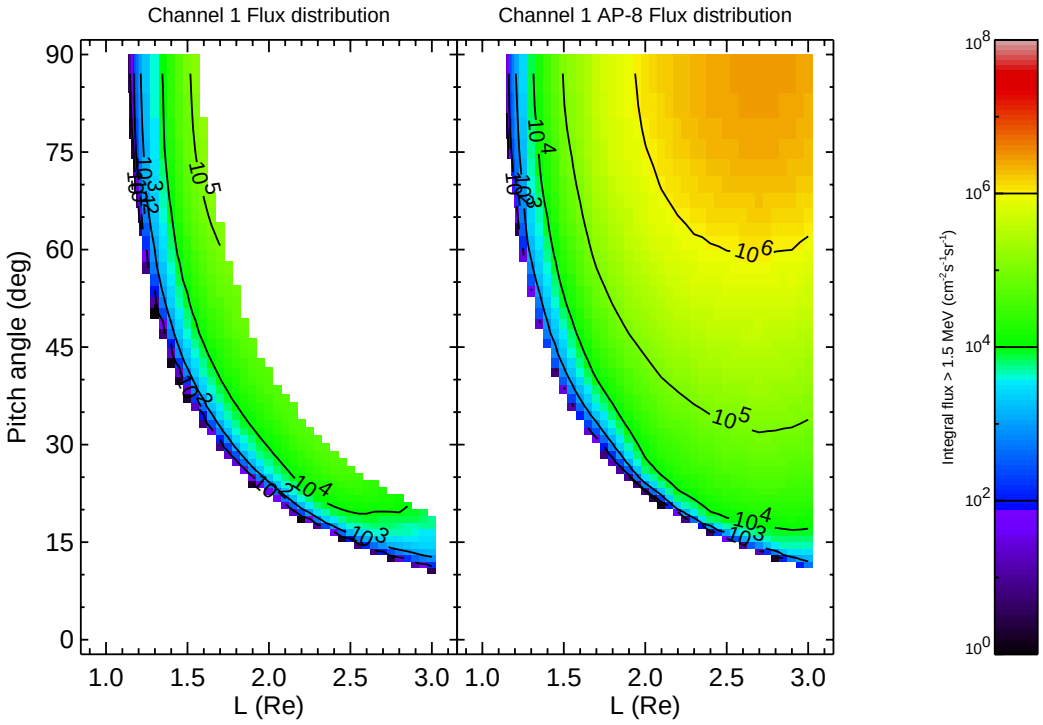

Figure 4.18. (L, α_0) Map of the PAB97 model and AP-8 MAX for channel 1

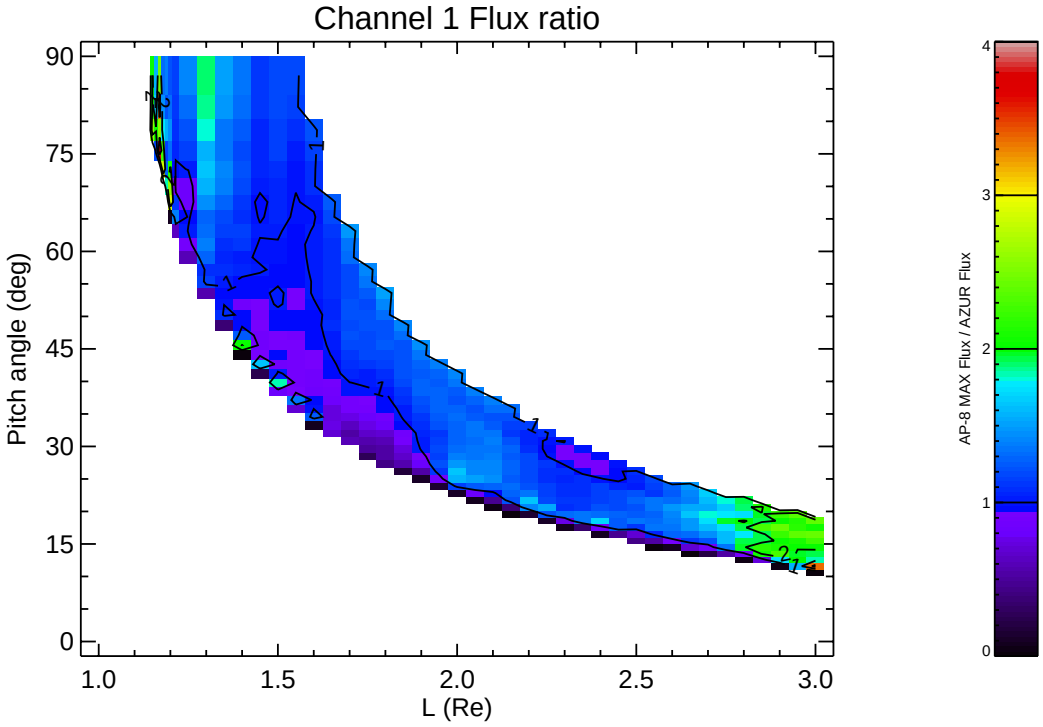

Figure 4.19. (L, α_0) Map of the ratio of AP-8 MAX to the PAB97 model for channel 1

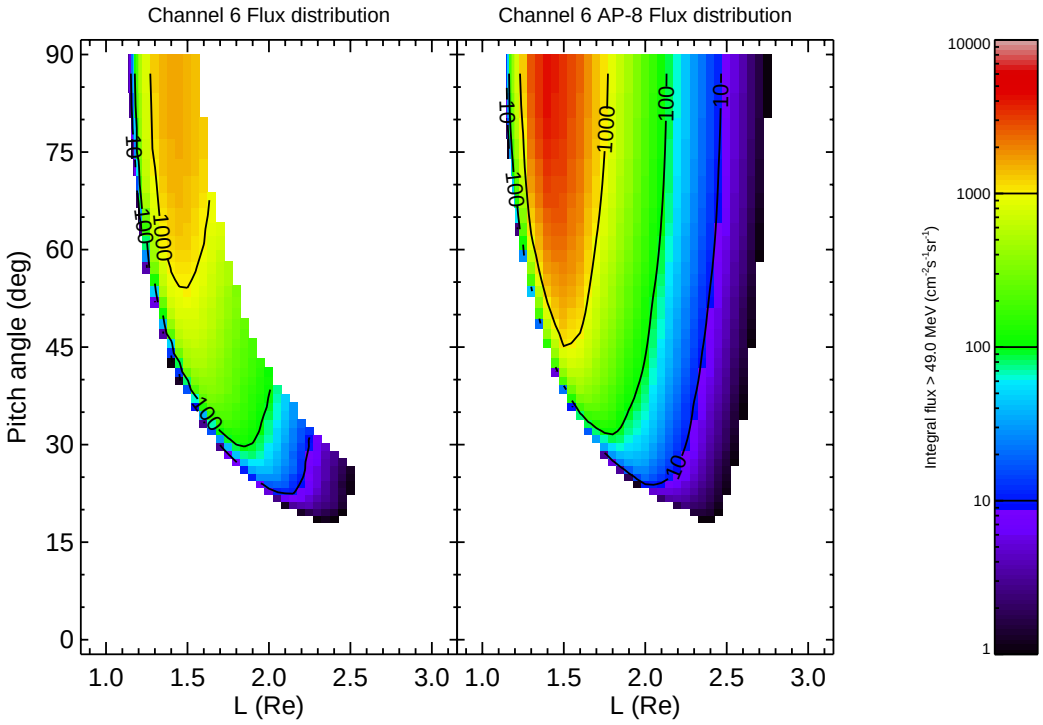

Figure 4.20. (L, α_0) Map of the PAB97 model and AP-8 MAX for channel 6

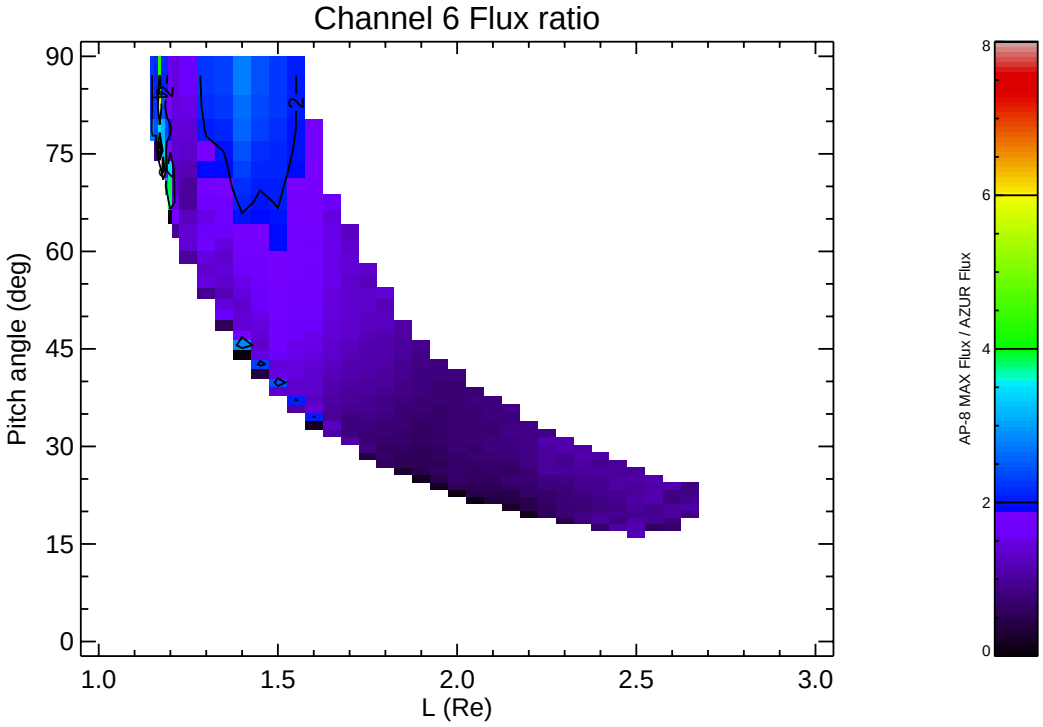

Figure 4.21. (L, α_0) Map of the ratio of AP-8 MAX to the PAB97 model for channel 6

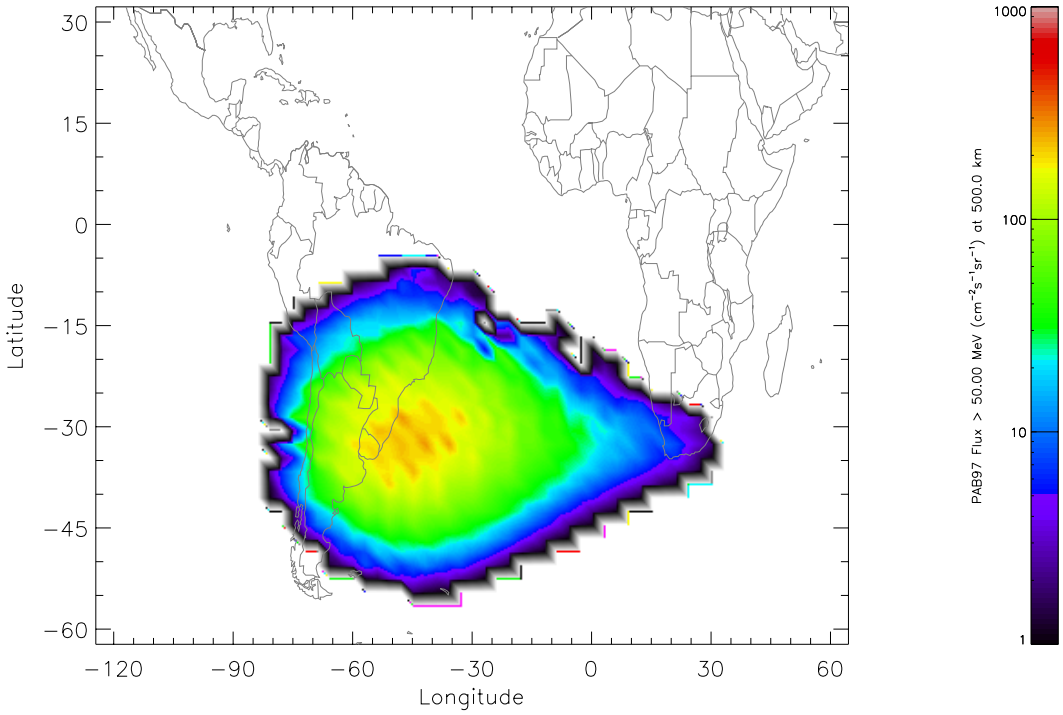

Figure 4.22. World map of the PAB97 >50 MeV proton flux at 500 km

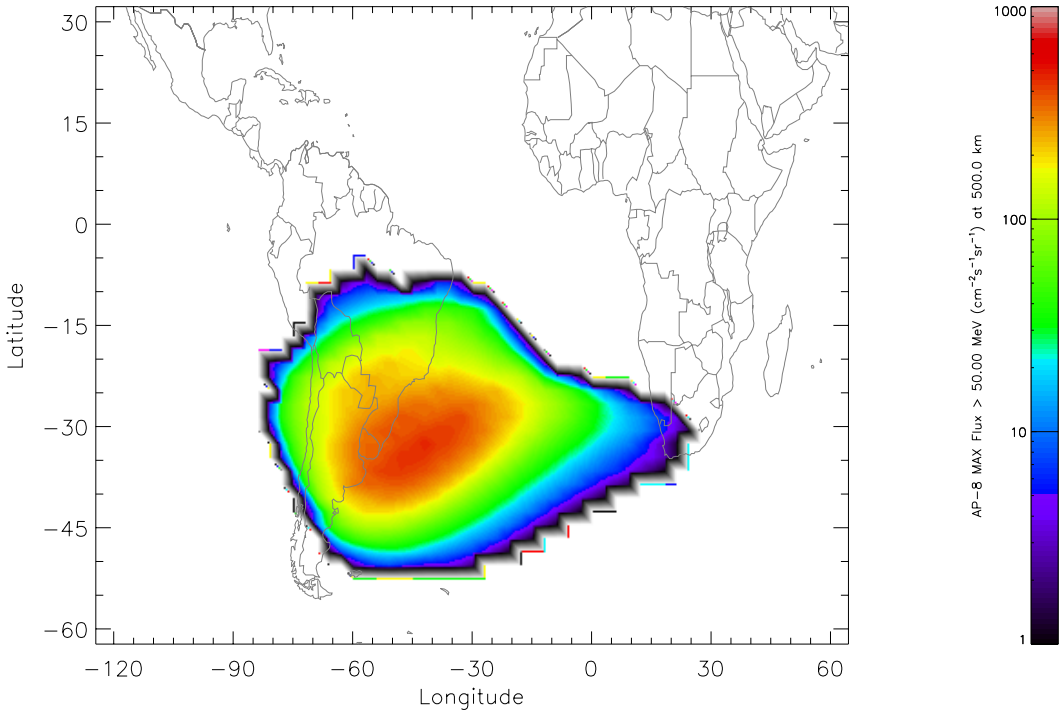

Figure 4.23. World map of the AP-8 MAX >50 MeV proton flux at 500 km